



Impact of compression on gas transport in non-woven gas diffusion layers of high temperature polymer electrolyte fuel cells



Dieter Froning^{a,*}, Junliang Yu^a, Gerd Gaiselmann^b, Uwe Reimer^a, Ingo Manke^c, Volker Schmidt^b, Werner Lehnert^{a,d}

^a Forschungszentrum Jülich GmbH, Institute of Energy and Climate Research, IEK-3: Electrochemical Process Engineering, D-52425 Jülich, Germany

^b Institute of Stochastics, Ulm University, Germany

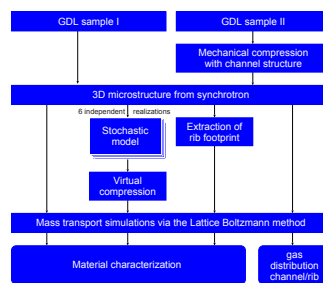
^c Helmholtz-Zentrum Berlin GmbH, Institute of Applied Materials, D-14109 Berlin, Germany

^d Modeling in Electrochemical Process Engineering, RWTH Aachen University, Germany

HIGHLIGHTS

- Detection of microstructure with synchrotron X-ray tomography.
- Mechanical compression of the microstructure.
- Virtual compression of a stochastic geometry model.
- Transport simulation with the Lattice Boltzmann method.

GRAPHICAL ABSTRACT



ARTICLE INFO

Article history:

Received 9 February 2016

Received in revised form

18 March 2016

Accepted 29 March 2016

Keywords:

HT-PEFC

GDL

Lattice Boltzmann

Stochastic modeling

ABSTRACT

Gas transport in non-woven gas diffusion layers of a high-temperature polymer electrolyte fuel cell was calculated with the Lattice Boltzmann method. The underlying micro structure was taken from two sources. A real micro structure was analyzed in the synchrotron under the impact of a compression mask mimicking the channel/rib structure of a flow field. Furthermore a stochastic geometry model based on synchrotron X-ray tomography studies was applied. The effect of compression is included in the stochastic model. Gas transport in these micro structures was simulated and the impact of compression was analyzed. Fiber bundles overlaying the micro structure were identified which affect the homogeneity of the gas flow. There are significant deviations between the impact of compression on effective material properties for this type of gas diffusion layers and the Kozeny-Carman equation.

© 2016 Elsevier B.V. All rights reserved.

1. Introduction

The knowledge of the characteristics of polymer electrolyte fuel cell (PEFC) components is essential for the efficient operation of fuel cells and stacks. It can be supported by mass transport

simulations at different spatial scales. The gas flow is often affected by material properties of the components. Gas diffusion layers (GDL) are used in low temperature PEFCs as well as in high temperature PEFCs (HT-PEFC) in order to distribute gases from the channels under the ribs of the flow field and collect the product gas on the cathode side. The transport characteristics of the GDL depend highly on the micro structure of the material which is of stochastic nature and can furthermore change under mechanical

* Corresponding author.

E-mail address: d.froning@fz-juelich.de (D. Froning).

compression. In former times, the effect of GDL was typically neglected in three dimensional (3D) cell and stack simulations [1]. But with increasing computational power the effect of GDL properties is often included [2]. Research groups are working on several fields covering the micro structure of the material and its characterization regarding mass transport and its impact on fuel cell applications. Experimental work and modeling of GDL complement one another in the development of PEFC and HT-PEFC. At this point, modeling of the micro structure [3–5] is often complemented by transport simulations. The micro structure of the material needs to be detected and transformed into geometry information to be used by the simulation software. The impact of transport characteristics on the fuel cell operation is of considerable evidence for the design of improved materials.

Experimental studies can follow various approaches. The permeability of GDLs was measured by Feser et al. [6] and also by Hussaini and Wang [7]. Taira and Liu [8] measured the effective permeability of GDL under the land region of a flow field. The general agreement of commonly used equations for permeability and tortuosity with visualizations of the micro structure of GDL was shown by Fishman and Bazylak [9]. The permeability of porous materials can be related to geometric properties for certain materials as shown by Tamayol et al. [10] and Hooman et al. [11] in their investigations on single phase gas transport in GDL. Several groups investigated liquid water distribution in operating PEFCs with neutron [12–14] and synchrotron X-ray imaging [15,16]. Experimental studies on the effect of compression on the performance of a PEFC were presented by Lee et al. [17]. Another kind of experiments was presented by Ye et al. [18] who investigated the bypass of water under the rib between two parallel gas flow channels. The GDL in their experiments was compressed by applying a defined tension to the flow field. A link between the micro structure of porous materials and its transport properties was presented by Koponen et al. [19]. Effective properties as permeability and tortuosity can be calculated from the flow fields resulting from Lattice Boltzmann (LB) simulations. This work bridges experimental work and simulations on both micro structures and cell level.

Various research groups are working on transport simulations in the micro structure of GDLs. Matyka et al. [20] calculated the tortuosity from streamlines which were obtained from two-dimensional LB simulations in randomly constructed porous structures. Thomas et al. [21] determined the accuracy of such results in relationship to the spatial discretization of the micro structure. Espinoza et al. [22] investigated the effect of compressed GDL on the permeability and tortuosity of a GDL with two-dimensional LB simulations. Gao et al. [23] focused on liquid water transport in GDL micro structures using three-dimensional LB simulations. Paper-type GDLs were reconstructed by Daino and Kandlikar [24] under consideration of the distribution of polytetrafluorethylene (PTFE) in the micro structure. Another stochastic geometry model [25] was taken by Froning et al. [26] to determine permeability and tortuosity of paper-type GDL represented by evaluating transport simulations in the micro structure. Through-plane and in-plane transport simulations using the Lattice Boltzmann method (LBM) were performed in micro structures under different levels of compression up to 50%. Nabovati et al. [27] calculated through-plane and in-plane permeability and tortuosity of reconstructed paper-type GDL using LB simulations. Under different conditions regarding homogeneous and heterogeneous porosity distributions they found higher in-plane permeabilities and lower in-plane tortuosities than the through-plane counterparts. Another kind of GDLs uses non-woven fleece, also made of carbon fibers. Su et al. [28,29] use this type of GDL in their investigations on polymer binder and platinum distribution in catalyst layers. Non-woven fiber based materials can have a more

complex micro structure which is also available for stochastic modeling. Gaiselmann et al. [30,31] investigated non-woven GDL from Freudenberg. They identified fiber bundles as superposed structures and incorporated them as a feature of their stochastic geometry model. Rama et al. [32] simulated gas transport in GDLs with the LBM in three-dimensional micro structures of woven carbon-cloth GDL from reconstructed X-ray micro-tomography which were compressed by applying dedicated weights to the GDL structure. They calculated pore sizes, porosity, permeability and tortuosity of woven GDLs under varying grades of compression. The anisotropy of the GDL as a function of compression was also presented.

Effective transport properties obtained from measurements or micro scale simulations can be used as model parameters in higher spatial scales. The presence of liquid water at low temperatures leads to different dominating effects for PEFC and HT-PEFC. In particular, Chippar et al. [33] studied the effect of GDL compression in PEFCs. They considered the impact of compression on effective transport properties of the GDL and the water saturation. Ju [34] studied the effect of anisotropy of the GDL on heat and water transport in a fuel cell. He investigated the anisotropy of the current density under the channel and under the rib crossways to the flow direction of a 0.5 mm wide channel. Hossain et al. [35] investigated the effect of GDL permeabilities on the efficiency of PEFC using a two-phase model. They observed high deterioration of the performance of a PEFC at low in-plane permeability of the GDL. Qi et al. [36] calculated the deformation of the GDL of a PEFC under mechanical compression. Bosomoiu et al. [37] investigated effective transport properties of fresh and aged GDL also under the land and channel regions of a flow field of a HT-PEFC. Chippar and Ju [38,39] modelled the gas crossover through the MEA of a HT-PEFC between a pair of fuel and gas channels of 1 mm width. The relevance of their investigations is affirmed by HT-PEFC stacks when they are assembled with meander type flow fields. Lüke et al. [40] measured the inhomogeneity of the current density distribution in a HT-PEFC stack with meander flow fields operated under several conditions.

In our paper we simulated gas transport in the micro structure of a GDL. The investigation was motivated by the research of Lüke et al. [40] and Kvesić et al. [41]. Their experiments on HT-PEFC stacks and corresponding Computational Fluid Dynamics (CFD) simulations showed the evidence of in-plane gas transport under the ribs of meander type flow fields. Liu et al. [42] presented a HT-PEFC with spiral flow fields which also benefits from in-plane gas transport under the ribs. To get insight into the underlying processes the micro structure of a Freudenberg GDL of type H2315 was investigated in the BESSY synchrotron by Tötze et al. [43]. From this micro structure a stochastic geometry model of the GDL was developed [44]. The geometry model can generate stochastic equivalent geometries of the uncompressed and compressed micro structure. Furthermore, the real micro structure was investigated in the BESSY synchrotron under the impact of compression by the ribs of the flow field on the micro structure. Transport simulations in these geometries were performed using the LBM. The effective transport properties permeability and tortuosity calculated from the results were analyzed. This numbers can be used for investigations of transport processes on cell and stack level [2,34,41]. Furthermore the inhomogeneous transport of gases under the ribs of the flow field was evaluated.

2. Methods

The micro structure of Freudenberg GDL (type H2315) was investigated in the BESSY synchrotron. The material was compressed virtually and also by a mechanical device according to Fig. 1 which depicts the processes of our investigations. Combining

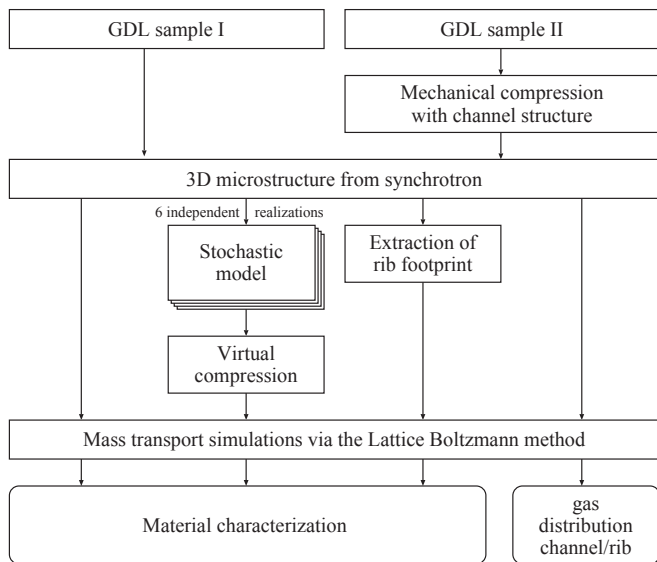


Fig. 1. Experimental and simulation scheme.

elements in our study of different GDL samples are the detection of the micro structure and transport simulations. Gas transport was simulated with the LBM and evaluated for material characterization and to locate inhomogeneities.

2.1. Detection of micro structure

Two GDL samples were investigated in the BESSY synchrotron. Sample I was used as a basis for the development of a geometry model of the micro structure. This is no. O in Table 1.

The three-dimensional data of the compressed material was used to generate a stochastic model of the micro structure as presented by Gaiselmann et al. [30]. Six realizations were created according Table 1 (no. A-F). The porosity of the uncompressed material was determined by counting black/white pixels in the representation of the chosen lattice. The porosity values of the six realizations of the stochastic model are close together. All realizations of the stochastic model were virtually compressed to enable transport simulations in 0% and 30% compressed material [31]. Realization no. F was used for all compression levels from 0 to 70%. 70% compression, e. g., stands for a total thickness of 30% of the original thickness of the material. The geometric structure is represented by a series of black/white (BW) images, each of them representing a layer of $0.833 \mu\text{m}$ thickness. The gray level images from the synchrotron were converted to BW for further processing.

Table 1

Uncompressed original micro structure (O), realizations of stochastic geometries (A-F) and real geometries under the rib (L, R; footprints in Fig. 3). The porosity is specified for the uncompressed material. X denotes available geometries.

GDL sample	No	Porosity /%	Compression/%									
			0	10	20	30	40	50	60	70		
I	O	76.5	X									
	A	76.4	X			X						
	B	76.1	X			X						
	C	76.7	X			X						
	D	76.1	X			X						
	E	76.3	X			X						
F	76.5	X	X	X	X	X	X	X	X	X	X	
II	L	77.0	X	X	X	X						
	R	77.0	X	X	X	X						

Fig. 2 shows a layer in the original structure and in a realization of the stochastic model. The images of size 1500 by 1500 build a section of $1.25 \text{ by } 1.25 \text{ mm}^2$ (Fig. 2). Every series of images contains of 240 layers representing a GDL thickness of $200 \mu\text{m}$ for the uncompressed material. The representation of the 70% compressed material still contains 72 images.

The GDL has a superposed structure built from fiber bundles which are considered by the stochastic model of the geometry. While the bundles cross the GDL plane in arbitrary direction they are favored in coordinate direction by the stochastic model. This can be seen in the upper left region of the right image in Fig. 2. The horizontal line is part of a fiber bundle which makes the modelled geometry stochastic equivalent to the real structure but it looks different at local positions. The fiber bundles build a superstructure with spatial dimensions in millimeter scale.

Sample II was compressed using a mechanical device introduced by Tötze et al. [43]. The compression device contained a mask with a channel/rib structure to represent the situation under the flow field of a fuel cell. Fig. 3 shows pieces of the real micro structure obtained from the BESSY synchrotron.

The images in Fig. 3 were taken from the gray level images from the synchrotron and converted into black/white images. The voxel size of the synchrotron images defined the spatial scale of the transport simulations. In this way every image is representing a layer of the GDL of $0.876 \mu\text{m}$ thickness. The images of size 2000 by 2000 show a GDL section of $1.75 \text{ by } 1.75 \text{ mm}^2$. Images close to the sample holder of the compression device show artifacts due to the manufacturing tolerance. Therefore a layer as close as possible to the sample holder was chosen as the basis layer. The chosen layer 0 (Fig. 3(a)) still shows some hint on the artifacts in the omitted images but it is dominated by the GDL structure as shown in the series of images in Fig. 3 which show the layers 0, 5, 10, and 15 steps of $0.876 \mu\text{m}$ towards the GDL structure. They show GDL micro structures which are not affected by external macro structures. But in this layers fiber bundles are hidden which are laid throughout the GDL micro structure similar as those from the other sample shown in Fig. 2. For the uncompressed case 268 images were available for the channel/rib scenario: layers 0 to 267. This includes 50 images where the GDL intrudes into the channel region. In the simulations of gas transport from the channel to the closed end of the structure the gas inlet is at layer 267, and layer 0 is the bottom layer at the GDL exit. At 10% compression 240 images were available, 224 images for 20% compression, and for 30% compression there were 197 images available for the channel/rib scenario. For the simulations on material characterization the section under the ribs were extracted – red frames in Fig. 3. Furthermore approx. 20 images were left out from the bottom of the images stack. In Fig. 3, the images (a) to (c) look more irregular than image (d). Therefore only 248 images were selected in the uncompressed case, 222 for 10% compression, 205 for 20% compression and 178 images were selected for the 30% compressed case.

2.2. Numerical transport simulations

The gas flow in the micro structure was simulated using the Lattice Boltzmann method. The open source software Palabos [45] was used with the BGK scheme and the D3Q19 discretization [46–48]. Three groups of transport simulations were run.

1. Effective transport properties were evaluated from transport simulations in real and stochastic geometries of sample I. This is according to lines O and A to F in Table 1.
2. The GDL under the ribs of the real structure from sample II was examined for effective transport properties. This is represented by lines L and R in Table 1.

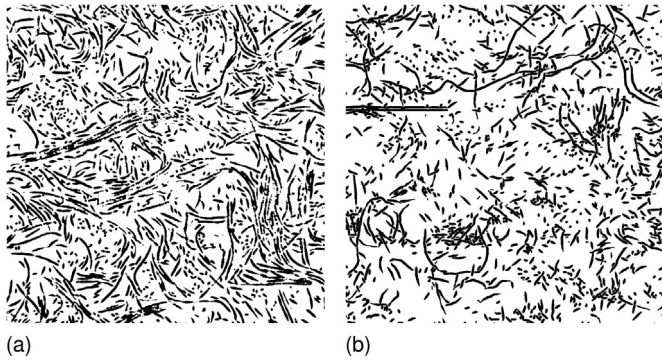


Fig. 2. Sample I: images of size 1500×1500 . (a) Original geometry, labelled (O) in Table 1, (b) realization (A) of the stochastic geometry model, uncompressed. Both of them: layer 105. GDL section of size 1.25 by 1.25 mm².

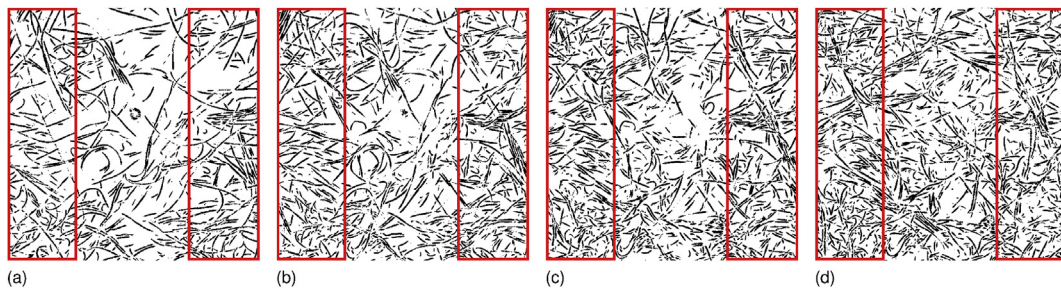


Fig. 3. Sample II: images of size 2000×2000 from the synchrotron after black/white conversion, uncompressed situation. GDL section of size 1.75 by 1.75 mm². Footprints of the ribs in red. (a) Layer 0, (b) layer 5, (c) layer 10, (d) layer 15. (For interpretation of the references to color in this figure legend, the reader is referred to the web version of this article.)

3. The gas transport under the rib of a flow field of sample II was investigated on real compressed GDL.

For the evaluation of effective transport properties of the stochastic geometries from Table 1, lines A–F, transport simulations were run similar as presented in Ref. [49]. Fig. 2 shows clearly that the stochastic geometry is not showing the real geometry exactly but it builds a micro structure which is equivalent to the real structure under stochastic view.

Like in previous studies [26,49], an empty space of 20 layers was added upstream and downstream to allow the definition of standard boundary conditions at the inlet and outlet without interfering with the irregular micro structure of the GDL. Inlet conditions were chosen with fixed velocity which was calculated from the total amount of hydrogen to be converted via Faraday's law under the assumption of a mean current density of 1 A cm^{-2} – also known as Dirichlet boundary condition. At the outlet, constant pressure was assumed which is known as a Neumann boundary condition on the velocity. At the four sides of the simulation domain wall boundary conditions were specified. The simulations were performed through-plane and in-plane. The in-plane simulations were run in two directions because the construction process of the GDL does not allow the assumption of properties being independent from the flow direction. Fig. 4 shows the simulation frame around a series of black/white images specifying the underlying micro structure. The annotation in the diagram is according to the through-plane situation.

Effective transport properties were also evaluated in real structures (sample II). For this purpose the compressed sections under the rib were extracted for transport simulations (Table 1, lines L, R). These regions were extracted as 550 by 2000 sections from the left (L) and right (R) side of each of the original 2000 by 2000

images.

For the evaluation of effective transport properties the transport was simulated in through-plane (x) direction and in two perpendicular in-plane directions (y, z). Because of superposed structures it cannot be assumed that the micro structure has isotropic in-plane conditions even under stochastic view [30,43].

Local behavior of the gas flow in the compressed micro structure of sample II was investigated by transport simulations in the real structure. The micro structure is represented by images of size 2000 by 2000 , each voxel of size $0.876 \mu\text{m}$. With this image series a section of 1.75 by 1.75 mm² is represented. The width of the channel structure is 890 pixels according to $780 \mu\text{m}$ (Fig. 3). This is a finer resolution than for sample I. According to Thomas et al. [21] a more accurate calculation of the pressure can be possible as long as other essential parameters do not change.

3. Results

3.1. Effective transport properties

Effective properties of the material were extracted from the simulation results of the homogeneous compressed real and stochastic geometries from Table 1, lines A–F. Similar as done in Ref. [26] the permeability κ was calculated from the velocity field via Darcy's law

$$\kappa = \frac{q \cdot \mu}{\nabla P} \quad (1)$$

In this equation q is the flux through the porous structure, and μ is the dynamic viscosity of the gas. ∇P is the pressure drop between the entry layer where the gas enters the GDL and the exit layer where the gas leaves it. The reciprocal value of κ can be used as a flow resistivity by porous media sub-models in CFD software. Kvesić et al. [41] used this approach with the ANSYS/Fluent software. Cao et al. [50], and Beale [51] used the same method for their CFD simulations of HT-PEFC with the open source software OpenFOAM. The tortuosity τ can be approximated by the approach according Koponen et al. [19].

$$\tau = \frac{\langle |v| \rangle}{\langle v_x \rangle} \quad (2)$$

Eq. (2) allows the calculation of the tortuosity from the velocity field of the transport simulation. $|v|$ is the absolute value of the velocity and v_x is its component in flow direction. $\langle \rangle$ denotes the spatial average over the region of interest, the GDL in our simulations. Eq. (2) was proven to be correct for capillary systems [19].

The tortuosity and permeability were also calculated in three directions of the real structure from under the rib in the channel/rib

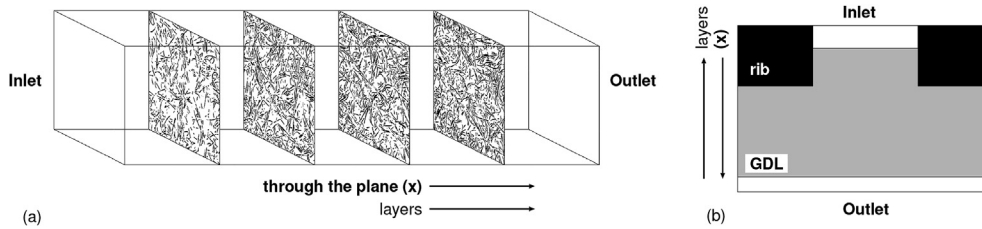


Fig. 4. Simulation frame of through-plane simulations. (a) Material characterization: Only four images of the micro structure are shown in the schematic view. The total number ranges from 72 to 240 for sample I and from 178 to 248 for sample II as described in Section 2.1. (b) Channel/rib scenario: The number of image layers ranges from 197 to 268.

scenario. In Table 1 this geometries are specified as L and R, denoting the left and right ribs.

The calculated effective values for permeability and tortuosity are shown in Table 2. In any cases the in-plane permeability in at least one of the two in-plane directions is approx. 50% higher than the through-plane permeability which is shown in the rightmost two columns where the in-plane permeabilities κ_1 and κ_2 were divided by the through-plane permeability κ_0 . This characteristic promotes the gas flow under the ribs of the flow field. This is in agreement with our previous results on paper-type GDL [26] and with the results of Nabovati et al. [27] who found the same tendency regarding in-plane and through-plane characteristics. The difference is that the in-plane characteristics of paper-type GDLs are independent from the in-plane direction *per definitionem*. The stochastic geometry model from Gaiselmann et al. [30] was fitted to 3D synchrotron data of the micro structure. It incorporates anisotropy of the in-plane properties of the GDL. The absolute permeability decreases under compression.

The most prominent property in Table 2 is the effective permeability which is depicted in Fig. 5(a). It shows results from simulations in real geometries from samples I and II and from realizations of the stochastic model from sample I. The through-plane permeability κ_0 and the in-plane permeabilities κ_1, κ_2 were given the same color for both samples I and II according to their directions. The vertical bars show the minimum and maximum values where they are available. For sample I, the largest difference in the min/max values are for κ_1 which is the in-plane permeability in the direction of the modelled fiber bundles. The GDL section analyzed in the synchrotron was not aligned to the orientation of the fiber bundles. Therefore the in-plane properties of the original data of sample I – entry O in Table 2 – are not aligned with those of the realizations A-F of the stochastic model. When in-plane characteristics become dominant for an application the MEA possibly might be assembled using a GDL rotated according to the orientation of the fiber bundles. For sample II the permeabilities in in-plane directions are not clearly separated according to their orientation because the coordinates of the simulation domain are not aligned with the orientation of the fiber bundles. The highest difference in the min/max values of the in-plane permeability is for κ_1 which is the direction of the shorter extent of the simulation domain (across the channel). Because of the domain size which is in the order of magnitude of the fiber bundles the behavior of the permeability is completely different from sample I.

It can be stated that the permeability values of the real geometry (L, R) differ from those of the stochastic geometries (A-F). The simulations on stochastic geometries show significant differences in the in-plane permeabilities κ_1 and κ_2 in the two directions along the coordinate axes. The reason is a superposed structure in the GDL material caused by the manufacture which can be seen in Fig. 3, layers 5 to 15. It shows that bundles of fibers are oriented approx. 30° skew to the top-down direction. This structure can also be observed in the resulting velocity profile in Fig. 7. The fiber

bundles are considered by the stochastic model of the geometry in the coordinate directions [30]. Therefore the impact of the fiber bundles on the material properties is pronounced by simulations on the stochastic geometries. In the real geometries (O, L, R) the fiber bundles are not oriented along coordinate axes. Therefore the in-plane transport properties κ and τ cannot be compared to those of the cases A-F. Moreover, the impact of the orientation of the fiber bundles on in-plane transport properties is smeared in simulations on the real geometry.

Like in our former investigations on another type of compressed GDL [26], we validated the transport simulations in the compressed micro structures according to the Kozeny-Carman trend. The permeability κ of a porous structure can be estimated from geometric properties by the Kozeny-Carman equation

$$\kappa = \frac{\varepsilon}{K_c} \left(\frac{V_p}{S_p} \right)^2. \quad (3)$$

The geometric properties in Eq. (3) are the porosity ε , the total volume V_p and the inner surface S_p . Tomadakis and Robertson [52] showed that the Kozeny constant K_c is related to the tortuosity τ

$$K_c = \tau \cdot \tilde{K}_c \quad (4)$$

with \tilde{K}_c depending only of the shape of the micro structure. Both equations lead to

$$\kappa \cdot \tau \sim \varepsilon \cdot \left(\frac{V_p}{S_p} \right)^2. \quad (5)$$

Tötzke et al. [43] stated that in case of homogeneous compression the fibers are mainly translated in through-plane direction. Supposed the shape of the micro structure does not change under compression, Eq. (5) can be used to estimate the term $\kappa \cdot \tau$ of compressed material based on its known value of uncompressed material via

$$\kappa \cdot \tau|_{x\%} = \kappa \cdot \tau|_{0\%} \cdot \varepsilon \left(\frac{V_p}{S_p} \right)^2|_{x\%} / \varepsilon \left(\frac{V_p}{S_p} \right)^2|_{0\%} \quad (6)$$

In Eq. (6) the notation $|_{0\%}$ specifies properties of the uncompressed material and $|_{x\%}$ denotes material with $x\%$ compression. Analyzing Eq. (6) leads to general expectations on the impact of $\kappa \cdot \tau$ under compression. While the volume V_p is reduced under compression the inner surface S_p should not change much under the assumption that the shape of the micro structure is kept. The total volume V_p decreases and also does the porosity ε as long as it is much larger than the compression. Then $\kappa \cdot \tau$ must decrease.

The simulated $\kappa \cdot \tau$ is shown in Fig. 5(b). The deviation of the simulated value from the Kozeny-Carman (KC) trend is summarized in Table 3.

The Kozeny-Carman trend $\kappa \cdot \tau|_{x\%}$ (Fig. 5(b)) of the stochastic geometries A-F of the compressed Freudenberg GDL decreases with

Table 2
Tortuosity τ and permeability κ of the stochastic geometries.

No.	Compression/ %	Through-plane		In-plane 1		In-plane 2		κ_1/κ_0	κ_2/κ_0
		τ	$\kappa_0/\mu\text{m}^2$	τ	$\kappa_1/\mu\text{m}^2$	τ	$\kappa_2/\mu\text{m}^2$		
O	0	1.207	6.67	1.158	9.74	1.149	9.97	1.46	1.49
A	0	1.208	10.85	1.138	15.64	1.170	12.07	1.44	1.11
B		1.216	9.95	1.144	14.75	1.174	11.80	1.48	1.19
C		1.209	10.64	1.131	16.11	1.168	12.68	1.51	1.19
D		1.217	10.17	1.135	15.09	1.179	12.34	1.48	1.21
E		1.203	10.28	1.144	13.87	1.181	12.10	1.35	1.18
F		1.211	10.46	1.136	15.24	1.167	12.98	1.46	1.24
A	30	1.271	4.70	1.196	7.82	1.241	5.78	1.66	1.23
B		1.278	4.05	1.228	6.95	1.253	5.29	1.72	1.31
C		1.263	4.55	1.180	8.22	1.241	6.04	1.80	1.33
D		1.275	4.23	1.186	6.89	1.253	6.06	1.63	1.43
E		1.255	4.30	1.206	6.28	1.286	5.62	1.46	1.31
F		1.271	4.50	1.190	7.17	1.239	6.08	1.59	1.35
F	0	1.211	10.46	1.136	15.24	1.167	12.98	1.46	1.24
	10	1.226	8.29	1.149	12.27	1.185	10.39	1.48	1.25
	20	1.246	6.30	1.166	9.60	1.207	8.13	1.52	1.29
	30	1.271	4.50	1.190	7.17	1.239	6.08	1.59	1.35
	40	1.302	2.93	1.225	4.96	1.283	4.29	1.69	1.46
	50	1.339	1.74	1.276	3.68	1.327	3.76	2.11	2.16
	60	1.367	0.76	1.367	1.73	1.399	2.36	2.27	3.09
	70	1.388	0.22	1.453	0.67	1.476	1.07	3.03	4.81
Average	0		10.39		15.12		12.33	1.45	1.19
A-F	30		4.39		7.22		5.81		
L	0	1.248	8.48	1.106	14.41	1.147	14.00	1.70	1.65
	10	1.235	8.63	1.106	12.71	1.162	12.04	1.47	1.40
	20	1.241	7.67	1.105	11.52	1.180	10.47	1.50	1.36
	30	1.249	6.22	1.103	9.76	1.163	9.82	1.57	1.58
R	0	1.264	7.62	1.115	13.10	1.145	13.63	1.72	1.79
	10	1.255	7.99	1.115	12.00	1.163	11.85	1.50	1.48
	20	1.257	7.17	1.115	10.71	1.180	10.44	1.49	1.46
	30	1.272	5.86	1.117	8.48	1.161	9.89	1.45	1.69

the compression and the curve has a convex shape. It shows the same behavior as the stochastic geometries of Toray GDL presented in Ref. [26] up to 40% compression which is the range of practical interest. In earlier transport simulations on paper-type GDLs [26] the deviation of $\kappa \cdot \tau$ from the Kozeny–Carmen trend increased with the compression level. At compression levels of 40% the deviations were less than 17.1% in through-plane direction. That is almost the same value as the deviation of the simulations of the F realization of Freudenberg GDL in Table 3. Hence, the transport simulations in stochastic geometries show a similar characteristic regarding the Kozeny–Carmen trend. The large deviation for higher compression levels reported in Table 3 can be a consequence of a conflict with the assumption of Eq. (6). For higher compression levels the fibers may touch each other and in consequence change the shape of the micro structure at this positions. It was also observed by Tötze et al. [43] that compression decreases the pore sizes in the micro structure but not the thickness of the fibers.

The situation for the values of sample II looks similar in Fig. 5(b) on the first view. The Kozeny–Carmen trend is close to the $\kappa \cdot \tau$ values but the shape of the curve looks concave. The deviation of the simulated $\kappa \cdot \tau$ values from the sections under the rib of sample II (L, R) is larger – especially for small amounts of compression. Moreover, the through-plane $\kappa \cdot \tau$ does not behave as expected from Eq. (6). Especially for the L case $\kappa \cdot \tau$ is even increasing from 0 to 10% compression. The simulations were run on sections 550 by 2000 which ranges from the outer border to the edge under the rib of the flow field. In Figs. 3 and 6 it is shown how the simulation domain of the L, R cases is specified by the footprint of the ribs. As the fiber bundles are crossing the edge of the rib the pre-condition of the Kozeny–Carman equation – the same shape of the uncompressed

and the compressed geometry – may possibly be violated. That may be a reason why the entries in lines L and R of Table 3 show a different trend as the stochastic geometries. Furthermore the superstructure built by the fiber bundles has similar spatial dimensions as the channel width. This shows the evidence of the size of the simulation domain for material characterization in presence of overlaid structures.

3.2. Channel/rib scenario

The simulation of the gas transport in the channel/rib scenario (sample II) was evaluated under the viewpoint of inhomogeneous mass transport. The results of the through-plane simulations in the channel/rib scenario were evaluated locally at the layer where the gas exits the GDL. Fig. 6 shows the through-plane component of the velocity field at the position where the gas leaves the GDL. Rightmost to the label '1' in the image there is a dark blue circle which coincides with a circular artifact shown in layer 0 of Fig. 3(a). The fibers left and right to the label '2' can be seen in layers 5 and 10 (Fig. 3(b),(c)) but not in layer 0. Hence, the lines in Fig. 6 are shadows of the real fibers nearby. The fiber right to the three labels '3' can be seen in layer 0 whereas the two lines nearby the two labels '4' are shadows of the fibers in layer 5 (Fig. 3(b)). The velocity field from Fig. 6 is evaluated with statistical methods. The x coordinate of the transport simulations is the through-plane direction. The y coordinate is across the channel, the z coordinate is along. The position across the channel is treated as independent stochastic variable. Every horizontal line was interpreted as a realization of gas transport in the stochastic material along the x coordinate, denoted as entities in Fig. 6. The velocity field in this layer looks

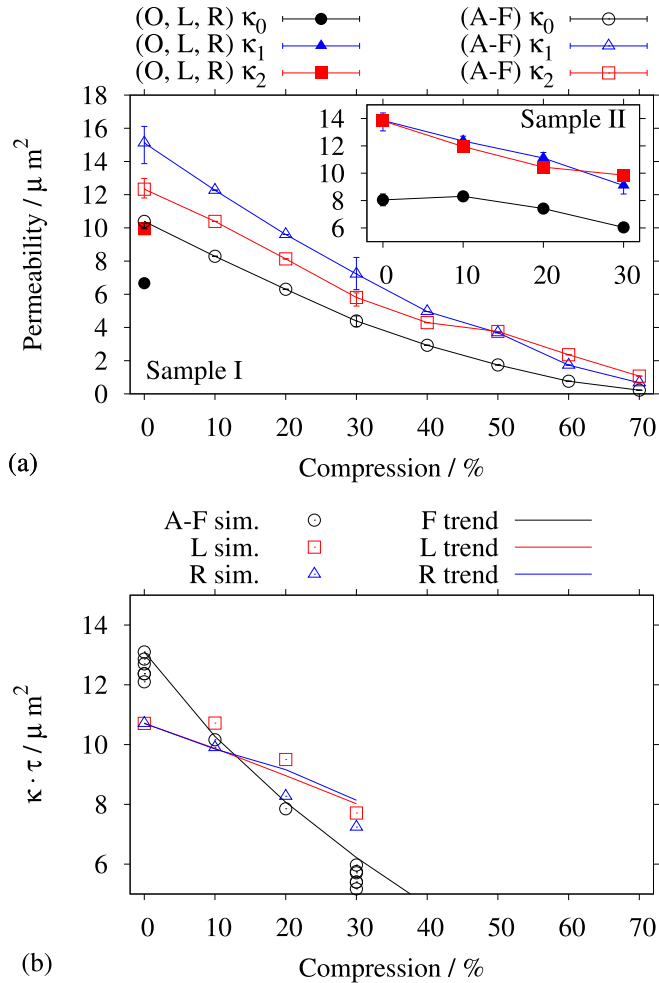


Fig. 5. (a) Effective permeability of the GDL samples. κ_0 : through-plane direction, κ_1, κ_2 : in-plane directions. Filled symbols: real geometries of samples I and II; outlined symbols: stochastic realizations of sample I. (b) Comparison of $\kappa \cdot \tau$ from transport simulations with the KC trend (Eq. (6)).

Table 3

Deviation/% of the through-plane simulations from the Kozeny-Carman trend $\kappa \cdot \tau|_{x\%}$ (Eq. (6)). Compression from 10 to 70% for realizations A-F, 10–30% for sections under the rib (L, R).

		Compression / %						
No.		10	20	30	40	50	60	70
A				6.9				
B				12.9				
C				8.6				
D				10.9				
E				10.3				
F		0.1	2.8	8.2	17.5	28.5	52.2	78.9
L		11.3	7.6	1.9				
R		13.2	9.5	1.9				

irregular on every compression level which is demonstrated by Fig. 7. This series of images show the situation of the gas flow at the position where the gas leaves the GDL. The image in Fig. 6 shows a section of 1.75 by 1.75 mm² with a 0.8 mm wide channel in the middle, and two ribs on the left and right side. The scale of the velocity in Fig. 6 ranges from 0 to 1.4 · 10⁻⁴ m s⁻¹. It is colored from blue (low) via white to red color (high). The fibers at this position are shown as dark blue shadows. They do not change under

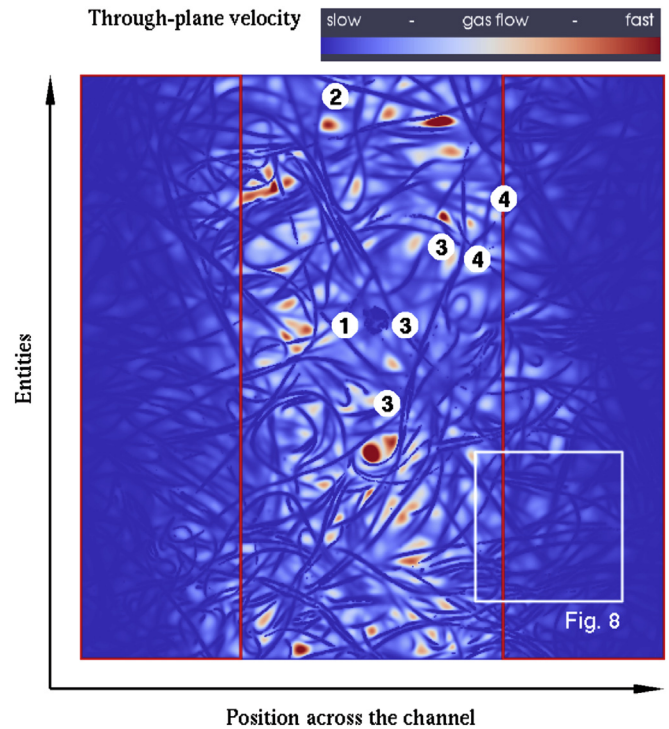


Fig. 6. Sample II: Through-plane velocity in the bottom layer of the uncompressed GDL in the channel/rib scenario. GDL section of size 1.75 by 1.75 mm². Footprint of the ribs in red. (For interpretation of the references to color in this figure legend, the reader is referred to the web version of this article.)

compression because the bottom level is fixed in the experimental setup. Fig. 7 enlarges the region marked by the white frame in Fig. 6. Fig. 7 shows (a) the uncompressed situation, and the situation under 10, 20, and 30% compression ((b), (c), (d)). The fibers at the bottom are visible on every image. With increasing compression fiber layers which were only visible as shadows under 0% compression come into the foreground. Furthermore, a separation of the velocity into bright and dark regions evolve under the edge of the rib. From left to right the brightness region left from the rib footprint increases while the colors at the right part under the rib become a little bit darker. But this effect has to be noted with care because this images represent only a very small region of the whole simulation domain.

A significant information in the channel/rib scenario is the amount of gas being transported under the rib of the flow field. For this purpose the resulting velocity field in the post processing layer is analyzed one-dimensional in y direction which is the abscissa in Fig. 6. The ordinate in the same diagram represents the entities measured at the y position across the channel. The entities are the number of observations which is the number of horizontal lines in the images of Figs. 6 and 7 in this case. They are weighted by the through-plane velocity of the gas in transport (x) direction. The velocities in the yz plane at the GDL exit are evaluated along the y coordinate as statistical density weighted by the velocity. This method simplifies the flow in the sense that winding paths of the real flow lines in the three dimensional micro structure – e. g., in order to flow around fibers – are neglected in y direction. To get statistical densities the weighted values need to be normalized because the integral must be equal to one. In particular, densities d_k , k denoting the grade of compression, can be calculated by the following approach.

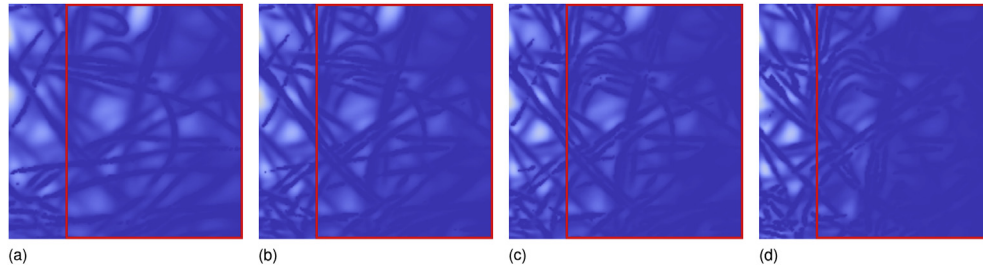


Fig. 7. Sample II: Through-plane velocity in a 500×500 section of the GDL exit layer. (a) Uncompressed, (b) 10% compression, (c) 20% compression, (d) 30% compression. GDL section of size 0.44 by 0.44 mm². Footprint of the rib in red. (For interpretation of the references to color in this figure legend, the reader is referred to the web version of this article.)

$$d_k(y) = \int_z v_x(y, z) dz \quad (7)$$

at the position y across the channel, velocity components v_x in transport direction, z being the along-the-channel direction. Weights w_k are chosen to ensure that $\int w_k \cdot d_k(y) dy = 1$ which makes the function $w_k d_k$ a statistical density. The resulting relative densities

$$\tilde{d}_k(y) = w_k \cdot d_k(y) / \overline{w_k \cdot d_k} \quad (8)$$

can be interpreted as relative velocities at a particular position across the channel as shown in Fig. 8. The average value of \tilde{d}_k is 1. The diagram shows a large variation in the velocity field across the channel. Though the variation across the channel is larger than the deviation between the curves a systematic impact of the compression can be stated. It is shown that the variation of the velocity across the channel does not change with compression since it is caused by the irregular micro structure. The velocity in the area under the channel is higher with increasing compression. The situation under the rib is reverse: the velocity decreases under compression. Stochastic evaluations of the flow field in the channel/rib scenario were performed with the R package [53].

From the one-dimensional density (Fig. 8) it can be calculated how much gas is transported under the ribs of the flow field structure. This can be done by evaluating the cumulated sum of the density shown in Fig. 8. The result in percentage is shown in Table 4.

The table shows that the transport of gases under the ribs is inhibited by the compression of the GDL caused from the ribs of the flow field. The mass transport under the left and the right rib is possibly affected by the superposed structure of the fiber bundles which is of similar size as the footprints of the ribs in our simulations.

4. Conclusion

Within this work the gas transport in non-woven type GDLs was simulated by using the Lattice-Boltzmann method. The geometric information was taken from three sources: 1) a real micro structure obtained from X-ray tomography, 2) a stochastic geometry model that allows for multiple generation of samples which are stochastically equivalent (i. e., from the same material), and 3) a real geometry of a channel/rib construction. The region under the rib was cut out for material characterization. The transport properties of uncompressed and compressed material were studied in view of effective permeability κ and tortuosity τ , both of them calculated from through-plane and in-plane transport simulations. The in-plane permeability is higher than the through-plane permeability in all cases. This information is useful in CFD simulations supporting the flow field design of HT-PEFC stacks.

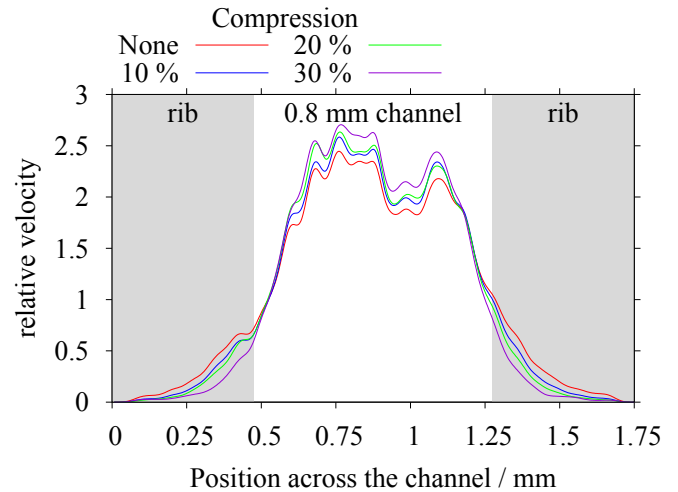


Fig. 8. Sample II: Density of the through-plane velocity at the GDL exit layer.

For compressed material the impact of compression on the product of the permeability and the tortuosity $\kappa \cdot \tau$ was evaluated in order to check the consistency of the simulation results. The trend which is expected according to the Kozeny-Carman equation could not be confirmed for this kind of non-woven GDLs. One possible explanation is the fact that the underlying super-structure of fiber bundles is on the same length scale as the size of the modeling domain of the smaller GDL sample.

A channel/rib scenario representing a repeating unit of the target application was analyzed qualitatively. The transport of gas under the ribs of the flow field is inhibited by the compressed micro structure of the GDL. Irregularities were found across the gas channel – possibly due to the superposed structure. For this kind of micro structure the impact of overlaid fiber bundles on the gas flow is larger than the impact of mechanical compression. This confirms the conclusion above that for material characterization the cross section of the simulation domain should be larger than the extent of relevant structures.

Table 4
Sample II: mass transfer under the ribs.

Compression %	Mass transfer under the ribs/%		
	Left	Right	Total
0	5.7	5.8	11.5
10	4.4	4.2	8.6
20	3.8	3.3	7.2
30	2.6	2.4	5.0

Acknowledgements

This research was partly funded by the German Federal Ministry of Education and Research Grant 05M10CJA. Simulations were performed on hardware of the Jülich Supercomputing Centre.

References

- [1] C. Siegel, Review of computational heat and mass transfer modeling in polymer-electrolyte-membrane (pem) fuel cells, *Energy* 33 (2008) 1331–1352.
- [2] A.Z. Weber, R.L. Borup, R.M. Darling, P.K. Das, T.J. Dursch, W. Gu, D. Harvey, A. Kusoglu, S. Litster, M.M. Mench, R. Mukundan, J.P. Owejan, J.G. Pharoah, M. Secanel, I.V. Zenyuk, A critical review of modeling transport phenomena in polymer-electrolyte fuel cells, *J. Electrochem. Soc.* 161 (2014) F1254–F1299.
- [3] R. Thiedmann, C. Hartnig, I. Manke, V. Schmidt, W. Lehnert, Local structural characteristics of pore space in GDLs of PEM fuel cells based on geometric 3D graphs, *J. Electrochem. Soc.* 156 (2009) B1339–B1347.
- [4] R. Thiedmann, I. Manke, W. Lehnert, V. Schmidt, Random geometric graphs for modelling the pore space of fibre-based materials, *J. Mater. Sci.* 46 (2011) 7745–7759.
- [5] G. Gaiselmann, R. Thiedmann, I. Manke, W. Lehnert, V. Schmidt, Stochastic 3D modeling of fiber-based materials, *Comput. Mater. Sci.* 59 (2012) 75–86.
- [6] J.P. Feser, A.K. Prasad, S.G. Advani, Experimental characterization of in-plane permeability of gas diffusion layers, *J. Power Sources* 162 (2006) 1226–1231.
- [7] I.S. Hussaini, C.Y. Wang, Measurement of relative permeability of fuel cell diffusion media, *J. Power Sources* 195 (2010) 3830–3840.
- [8] H. Taira, H. Liu, In-situ measurements of gdl effective permeability and under-land cross-flow in a pem fuel cell, *Int. J. Hydrogen Energy* 37 (2012) 13725–13730.
- [9] Z. Fishman, A. Bazylak, Heterogeneous through-plane distributions of tortuosity, effective diffusivity, and permeability for PEMFC GDLs, *J. Electrochem. Soc.* 158 (2011) B247–B252.
- [10] A. Tamayol, F. McGregor, M. Bahrami, Single phase through-plane permeability of carbon paper gas diffusion layers, *J. Power Sources* 204 (2012) 94–99.
- [11] K. Hooman, A. Tamayol, M. Dahari, M. Safaei, H. Togun, R. Sadri, A theoretical model to predict gas permeability for slip flow through a porous medium, *Appl. Therm. Eng.* 70 (2014) 71–76.
- [12] A. Schröder, K. Wippermann, J. Mergel, W. Lehnert, D. Stolten, T. Sanders, T. Baumhöfer, D.U. Sauer, I. Manke, N. Kardjilov, A. Hilger, J. Schloesser, J. Banhart, C. Hartnig, Combined local current distribution measurements and high resolution neutron radiography of operating direct methanol fuel cells, *Electrochem. Commun.* 11 (2009) 1606–1609.
- [13] A. Schröder, K. Wippermann, W. Lehnert, D. Stolten, T. Sanders, T. Baumhöfer, N. Kardjilov, A. Hilger, J. Banhart, I. Manke, The influence of gas diffusion layer wettability on direct methanol fuel cell performance: a combined local current distribution and high resolution neutron radiography study, *J. Power Sources* 195 (2010) 4765–4771.
- [14] A.D. Santamaria, M.K. Becton, N.J. Cooper, A.Z. Weber, J.W. Park, Effect of cross-flow on pefc liquid-water distribution: an in-situ high-resolution neutron radiography study, *J. Power Sources* 293 (2015) 162–169.
- [15] I. Manke, M. Grünerbel, W. Lehnert, N. Kardjilov, A. Haibel, A. Hilger, J. Banhart, H. Riesemeier, Investigation of water evolution and transport in fuel cells with high resolution synchrotron x-ray radiography, *Appl. Phys. Lett.* 90 (2007) 174105.
- [16] W. Maier, T. Arlt, C. Wannek, I. Manke, H. Riesemeier, P. Krüger, J. Scholta, W. Lehnert, J. Banhart, D. Stolten, In-situ synchrotron X-ray radiography on high temperature polymer electrolyte fuel cells, *Electrochem. Commun.* 12 (2010) 1436–1438.
- [17] W.-K. Lee, C.-H. Ho, J.W. van Zee, M. Murthy, The effects of compression and gas diffusion layers on the performance of a PEM fuel cell, *J. Power Sources* 84 (1999) 45–51.
- [18] D.H. Ye, E. Gauthier, M.J. Cheah, J. Benziger, M. Pan, The effect of gas diffusion layer compression on gas bypass and water slug motion in parallel gas flow channels, *AIChE J.* 61 (2015) 355–367.
- [19] A. Koponen, M. Kataja, J. Timonen, Tortuous flow in porous media, *Phys. Rev. E* 54 (1996) 406–410.
- [20] M. Matyka, A. Khalili, Z. Koza, Tortuosity-porosity relation in porous media flow, *Phys. Rev. E* 78 (2008) 026306.
- [21] M.L.R. Thomas, D.B. Ingham, M. Pourkashanian, Prediction of the permeability of fibrous media using the Lattice Boltzmann method in conjunction with coarse numerical lattices, *Open Transp. Phenom. J.* 2 (2010) 80–89.
- [22] M. Espinoza, M. Andersson, J. Yuan, B. Sundén, Compress effects on porosity, gas-phase tortuosity, and gas permeability in a simulated pem gas diffusion layer, *Int. J. Energy Res.* 39 (2015) 1528–1536.
- [23] Y. Gao, X. Zhang, P. Rama, R. Chen, H. Ostadi, K. Jiang, Lattice Boltzmann simulation of water and gas flow in porous gas diffusion layers in fuel cells reconstructed from micro-tomography, *Comput. Math. Appl.* 65 (2013) 891–900.
- [24] M.M. Daino, S.G. Kandlikar, 3D phase-differentiated GDL microstructure generation with binder and PTFE distributions, *Int. J. Hydrogen Energy* 37 (2012) 5180–5189.
- [25] R. Thiedmann, F. Fleischer, C. Hartnig, W. Lehnert, V. Schmidt, Stochastic 3D modeling of the GDL structure in PEMFCs based on thin section detection, *J. Electrochem. Soc.* 155 (2008) B391–B399.
- [26] D. Froning, J. Brinkmann, U. Reimer, V. Schmidt, W. Lehnert, D. Stolten, 3D analysis, modeling and simulation of transport processes in compressed fibrous microstructures, using the Lattice Boltzmann method, *Electrochim. Acta* 110 (2013) 325–334.
- [27] A. Nabovati, J. Hinebaugh, A. Bazylak, C.H. Amon, Effect of porosity heterogeneity on the permeability and tortuosity of gas diffusion layers in polymer electrolyte membrane fuel cells, *J. Power Sources* 248 (2014) 83–90.
- [28] H. Su, S. Pasupathi, B. Bladergroen, V. Linkov, B.G. Pollet, Optimization of gas diffusion electrode for polybenzimidazole-based high temperature proton exchange membrane fuel cell: evaluation of polymer binders in catalyst layer, *Int. J. Hydrogen Energy* 38 (2013) 11370–11378.
- [29] H. Su, H. Liang, B.J. Bladergroen, V. Linkov, B.G. Pollet, S. Pasupathi, Effect of platinum distribution in dual catalyst layer structured gas diffusion electrode on the performance of high temperature PEMFC, *J. Electrochem. Soc.* 161 (2014) F506–F512.
- [30] G. Gaiselmann, D. Froning, C. Tötze, C. Quick, I. Manke, W. Lehnert, V. Schmidt, Stochastic 3D modeling of non-woven materials with wet-proofing agent, *Int. J. Hydrogen Energy* 38 (2013) 8448–8460.
- [31] G. Gaiselmann, C. Tötze, I. Manke, W. Lehnert, V. Schmidt, 3D microstructure modeling of compressed fiber-based materials, *J. Power Sources* 257 (2014) 52–64.
- [32] P. Rama, Y. Liu, R. Chen, H. Ostadi, K. Jiang, Y. Gao, X. Zhang, D. Brivio, P. Grassini, A numerical study of structural change and anisotropic permeability in compressed carbon cloth polymer electrolyte fuel cell gas diffusion layers, *Fuel Cells* 11 (2011) 274–285.
- [33] P. Chippa, K.O.K. Kang, H. Ju, A numerical investigation of the effects of gdl compression and intrusion in polymer electrolyte fuel cells (pefcs), *Int. J. Hydrogen Energy* 37 (2012) 6326–6338.
- [34] H. Ju, Investigation of the effects of the anisotropy of gas-diffusion layers on heat and water transport in polymer electrolyte fuel cells, *J. Power Sources* 191 (2009) 259–268.
- [35] M. Hossain, S.Z. Islam, P. Pollard, Investigation of species transport in a gas diffusion layer of a polymer electrolyte membrane fuel cell through two-phase modelling, *Renew. Energy* 51 (2013) 404–418.
- [36] L. Qi, K. Jiao, A. Pereira, X. Li, 3D multiphase modeling of PEMFC with uneven compression of GDL, *ECS Trans.* 28 (2010) 259–271.
- [37] M. Bosomoiu, G. Tsotridis, T. Bednarek, Study of effective transport properties of fresh and aged gas diffusion layers, *J. Power Sources* 285 (2015) 568–579.
- [38] P. Chippa, H. Ju, Three-dimensional non-isothermal modeling of a phosphoric acid-doped polybenzimidazole (PBI) membrane fuel cell, *Solid State Ion.* 225 (2012) 30–39.
- [39] P. Chippa, H. Ju, Numeric modeling and investigation of gas crossover effects in high temperature proton exchange membrane (PEM) fuel cells, *Int. J. Hydrogen Energy* 38 (2013) 7704–7714.
- [40] L. Lücke, H. Janßen, M. Kvesić, W. Lehnert, D. Stolten, Performance analysis of HT-PEFC stacks, *Int. J. Hydrogen Energy* 37 (2012) 9171–9181.
- [41] M. Kvesić, U. Reimer, D. Froning, L. Lücke, W. Lehnert, D. Stolten, 3D modeling of a 200 cm² HT-PEFC short stack, *Int. J. Hydrogen Energy* 37 (2012) 2430–2439.
- [42] F. Liu, M. Kvesić, K. Wippermann, U. Reimer, W. Lehnert, Effect of spiral flow field design on performance and durability of HT-PEFCs, *J. Electrochem. Soc.* 160 (2013) F892–F897.
- [43] C. Tötze, G. Gaiselmann, M. Osenberg, J. Böhner, T. Arlt, M. Markötter, A. Hilger, F. Wieder, A. Kupsch, B.R. Müller, M.P. Hentschel, J. Banhart, V. Schmidt, W. Lehnert, I. Manke, Three-dimensional study of compressed gas diffusion layers using synchrotron X-ray imaging, *J. Power Sources* 253 (2014) 123–131.
- [44] G. Gaiselmann, I. Manke, W. Lehnert, V. Schmidt, Extraction of curved fibers from 3D data, *Image Anal. Stereol.* 32 (2013) 57–63.
- [45] Palabos, <http://www.palabos.org/>, Nov 14, 2012.
- [46] S. Succi, *The Lattice Boltzmann Equation*, Oxford University Press, Oxford, 2001.
- [47] D. Hänel, *Molekulare Gasdynamik*, Springer, 2004.
- [48] D. Wolf-Gladrow, *Lattice-Gas Cellular Automata and Lattice Boltzmann Models*, Springer, Berlin, 2000.
- [49] D. Froning, G. Gaiselmann, U. Reimer, J. Brinkmann, V. Schmidt, W. Lehnert, Stochastic aspects of mass transport in gas diffusion layers, *Transp. Porous Media* 103 (2014) 469–495.
- [50] Q. Cao, S.B. Beale, U. Reimer, D. Froning, W. Lehnert, The importance of diffusion mechanisms in high temperature polymer electrolyte fuel cells, *ECS Trans.* 69 (2015) 1089–1103.
- [51] S.B. Beale, Mass transfer formulation for polymer electrolyte membrane fuel cell cathode, *Int. J. Hydrogen Energy* 40 (2015) 11641–11650.
- [52] M.M. Tomadakis, T.J. Robertson, Viscous permeability of random fiber structures: comparison of electrical and diffusional estimates with experimental and analytical results, *J. Compos. Mater.* 39 (2005) 163–188.
- [53] R Core Team, *R: A Language and Environment for Statistical Computing*, R Foundation for Statistical Computing, 2013. Vienna, Austria.